

An Unbiased Estimator of the Full-sky CMB Angular Power Spectrum using Neural Networks

Pallav Chanda^{*1} and Rajib Saha^{†2}

^{1, 2}Department of Physics, Indian Institute of Science Education and Research, Bhopal

February 8, 2021

Abstract

Accurate estimation of the Cosmic Microwave Background (CMB) angular power spectrum is enticing due to the prospect for precision cosmology it presents. Galactic foreground emissions, however, contaminate the CMB signal and need to be subtracted reliably in order to lessen systematic errors on the CMB temperature estimates. Typically bright foregrounds in a region lead to further uncertainty in temperature estimates in the area even after some foreground removal technique is performed and hence determining the underlying full-sky angular power spectrum poses a challenge. We explore the feasibility of utilizing artificial neural networks to predict the angular power spectrum of the full sky CMB temperature maps from the observed angular power spectrum of the partial sky in which CMB temperatures in some bright foreground regions are masked. We present our analysis at large angular scales with two different masks. We produce unbiased predictions of the full-sky angular power spectrum and the underlying theoretical power spectrum using neural networks. Our predictions are also uncorrelated to a large extent. We further show that the multipole-multipole covariances of the predictions of the full-sky spectra made by the ANNs are much smaller than those of the estimates obtained using the method of pseudo- C_l .

1 Introduction

The Cosmic Microwave Background (CMB) is considered as an important probe of the early universe. Details regarding the cosmological parameters, obtained from the angular power spectrum of the CMB temperature and polarization anisotropies, have proved useful in understanding the mechanism for the formation and the growth of large-scale structure. Constraints on cosmological parameters have been obtained by satellite-based experiments like COBE [1], WMAP [2], and PLANCK [3], as well as ground-based experiments like ACT [4], and SPT [5]. Upcoming projects like the CCAT-prime [6], ESA CORE [7], and others with improved sensitivities and specialized equipment, will surely make remarkable improvements in CMB measurements.

The CMB, discovered in 1965 [8], is a nearly-uniform and isotropic radiation field exhibiting a virtually perfect black-body spectrum at a temperature of 2.7255K [9] with minute fluctuations, called temperature anisotropies, of the order of μK . During an observation, the temperature fluctuations are seen projected on the 2D surface of the spherical sky. Therefore, the temperature anisotropies can be expressed by using a spherical harmonic expansion as follows:

$$T(\theta, \phi) = \sum_{l=0}^{\infty} \sum_{m=-l}^l a_{lm} Y_{lm}(\theta, \phi), \quad (1)$$

where $Y_{lm}(\theta, \phi)$ are the spherical harmonic functions, and

a_{lm} are the harmonic modes given by,

$$a_{lm} = \int_{\theta=-\pi}^{\pi} \int_{\phi=0}^{2\pi} T(\theta, \phi) Y_{lm}^*(\theta, \phi) d\Omega. \quad (2)$$

Noting that one can measure only $(2l+1)$ m -modes for a multipole, the angular power spectrum can be written as,

$$\hat{C}_l = \frac{1}{2l+1} \sum_{m=-l}^l |a_{lm}|^2. \quad (3)$$

\hat{C}_l is χ^2 -distributed with a mean of C_l^{th} , a variance of $2(C_l^{\text{th}})^2/(2l+1)$, and $2l+1$ degrees of freedom, where C_l^{th} represents the theoretical power spectrum. Therefore,

$$C_l^{\text{th}} = \langle \hat{C}_l \rangle = \frac{1}{2l+1} \sum_{m=-l}^l \langle |a_{lm}|^2 \rangle, \quad (4)$$

where $\langle \circ \rangle$ denotes an ensemble average. Since we have only one real sky, our observation of the CMB sky will be described by one such realization of the angular power spectrum drawn from the above-stated distribution.

The statistical information present in a CMB temperature anisotropy map can be encapsulated in its angular power spectrum, \hat{C}_l , in the widely accepted structure formation model of inflation-introduced curvature perturbations that are Gaussian-distributed. Extracting cosmological information from CMB observations is possible only when all non-cosmological signals are reliably subtracted. Recent CMB experiments are equipped with adequate angular resolution and sensitivity to probe CMB anisotropies

^{*}email: pallav16@iiserb.ac.in

[†]email: rajib@iiserb.ac.in

at large angular scales. Therefore, the primary source of uncertainty in estimates is due to the galactic foreground emissions and not the instrumental noise.

The galactic foregrounds are characterized by much higher intensities (temperatures) in the region around the galactic plane compared to other regions on the sky. This results in comparatively higher uncertainties in CMB measurements in those regions when reconstructed using existing methods like COMMANDER (see Eriksen et al. 2004 [10], Eriksen et al. 2008 [11]), ILC (see Saha et al. 2006, 2008 [12, 13], Sudevan et al. 2018 [14]), etc. Bright sources in some sky regions also result in further unreliability of the measurements. Applying a mask on the CMB temperature map, that excludes the components in ‘bright’ foreground regions, aids data analysis. The angular power spectrum of the partial (masked) sky can then be computed easily. However, recovering an unbiased estimator of the underlying full-sky angular power spectrum is an important problem in cosmology to solve.

Common maximum likelihood methods [15, 16], Gibbs and Bayesian sampling methods [10, 17] exist for estimating the full-sky CMB temperature anisotropy angular power spectrum, \hat{C}_l , from the angular power spectrum of finite-area cut-sky CMB map, \hat{C}_l . However, these methods involve complex computations and are CPU expensive since they scale as l_{\max}^6 , with l_{\max} being the maximum multipole. The method using Gabor transforms, introduced by Hansen et al. (2002) [18], is again hindered by slow calculations of the correlation matrix of \hat{C}_l needed for their maximum likelihood analysis.

Furthermore, Peebles (1973) [19], Wandelt et al. (2001) [20] and Hivon et al. (2002) [21] put forward the pseudo- C_l algorithm for estimation of the full-sky angular power spectrum from the masked-sky spectrum, which foregoes the slow calculations by introducing a mode-mode coupling kernel that depends only on the geometry of the mask used. Various extensions of the pseudo- C_l method exist like those presented by Reinecke et al. (2013) [22], Elsner et al. (2017) [23], and the references therein. Nevertheless, the \hat{C}_l estimates using these methods have large error-bars on the low multipoles, even after using substantial bin-width, and are also limited in the sense that the unbiased estimator relies on a linear transformational relation that exists between the ensemble averages, $\langle \hat{C}_l \rangle$ and $\langle \hat{C}_l \rangle$, which may not necessarily be the best possible relation between \hat{C}_l and \hat{C}_l of the individual realizations. Therefore, the requirement for a technique that is efficient, reliable, and enables optimal recovery of the full-sky angular power spectra at all multipoles is well documented.

In this work, we have explored the use of Artificial Neural Networks (ANNs) to predict the full-sky CMB angular power spectrum based on the power spectrum of the partial (or masked) sky as a new alternative method. We are interested in the reconstruction of large-scale CMB temperature anisotropy power spectrum in this initial article. We produce random realizations of the CMB temperature anisotropy, i.e., CMB maps. We choose the suitable temperature masks to apply on the CMB maps so as to get the masked CMB maps. Then, we calculate the angular power spectra of the masked CMB maps as well as the un-

masked (full-sky) CMB maps, hereafter represented as \hat{C}_l s and \hat{C}_l s respectively. The simulated data is used to construct training and testing sets for the ANNs. The training data plays a role similar to that of the priors and is used by the neural network to learn the complicated mapping that exists between the \hat{C}_l and \hat{C}_l of the individual realizations. ANNs are well-known as universal function approximators (see Hornik (1991) [24], Pinkus (1999) [25]). Using this novel method enables us to get unbiased predictions of the full-sky spectra without binning at lower multipoles and with a minimal bin width at higher multipoles. We also obtain significantly smaller error-bars on our full-sky \hat{C}_l predictions. The ANN predictions help us acquire an unbiased estimator of the underlying theoretical C_l^{th} as well.

This paper is organized as follows: In §2, we derive the necessary equations that relate the the full-sky angular power spectrum to the partial-sky power spectrum. Next, we give a brief review of the concept of Artificial Neural Networks in §3. In §4, we present our strategy for getting an unbiased estimate of the full-sky angular power spectrum from the power spectrum of the partial-sky. §5 describes the process for simulating the CMB maps, the corresponding \hat{C}_l s and the \hat{C}_l s. We list our methodology, the procedure for training the networks, and the binning strategy required to get an unbiased estimate after making the predictions in §6. In §7, we present the results of our analyses on the simulated data. Our conclusions and possible future work on our method are discussed in §8.

2 From Partial-sky to the Full-sky Power Spectrum

The effects of a mask on the full-sky temperature field can be described by a position-dependent weighting using a window function W . The effect of a finite window function on the temperature field is given by,

$$\tilde{T}(\theta, \phi) = W(\theta, \phi)T(\theta, \phi). \quad (5)$$

Defining the harmonic space window function, $W_{lm}^{l'm'}$, as:

$$W_{lm}^{l'm'} = \int_{\theta=-\pi}^{\pi} \int_{\phi=0}^{2\pi} Y_{l'm'}(\theta, \phi)W(\theta, \phi)Y_{lm}^*(\theta, \phi)d\Omega, \quad (6)$$

the harmonic modes of the partial (masked) sky are given by,

$$\tilde{a}_{lm} = \sum_{l'm'} W_{lm}^{l'm'} a_{l'm'}. \quad (7)$$

Using these harmonic modes, the angular power spectrum of the masked sky can be calculated as,

$$\hat{C}_l = \frac{1}{2l+1} \sum_{m=-l}^l |\tilde{a}_{lm}|^2. \quad (8)$$

Thus, one can relate the partial-sky power spectra to the full-sky spectra by taking ensemble averages on both sides and then using Eq.7 and Eq.4 as follows:

$$\begin{aligned} \langle \hat{C}_l \rangle &= \frac{1}{2l+1} \sum_{m=-l}^l \langle \tilde{a}_{lm} \tilde{a}_{lm}^\dagger \rangle \\ &= \sum_{l'} \sum_{mm'} W_{lm}^{l'm'} \langle \hat{C}_{l'} \rangle (W_{lm}^{l'm'})^\dagger. \end{aligned} \quad (9)$$

The above expression can be simplified by using a matrix M to describe the mode-mode coupling, and it becomes:

$$\langle \hat{\tilde{C}}_l \rangle = \sum_{l'} M_{ll'} \langle \hat{C}_{l'} \rangle. \quad (10)$$

On the large scales that we are working on, the instrumental noise is negligible in magnitude and hence, can be ignored. Thus, inverting Eq.10, the true full-sky power spectra can be represented in terms of the pseudo partial-sky spectra,

$$\langle \hat{C}_l \rangle = \sum_{l'} M_{ll'}^{-1} \langle \hat{\tilde{C}}_{l'} \rangle. \quad (11)$$

For a given realization of the CMB sky, we use the convention that \mathbf{c} represents the column vector whose elements are the \hat{C}_l ($l = 0, 1, \dots, l_{\max}$) and $\tilde{\mathbf{c}}$ represents the column vector whose elements are the $\hat{\tilde{C}}_l$ ($l = 0, 1, \dots, l_{\max}$), where, l_{\max} depends on the resolution of the temperature maps, throughout the paper. If the ensemble averages in Eq.11 are eliminated, the same relation can be used as an estimator of the full-sky CMB \hat{C}_l using the partial-sky $\hat{\tilde{C}}_l$. This relation is key to the existing pseudo- C_l methods. However, the linear transformational relation holds only on the stated ensemble averages and thus, inherently, excludes the complex functional relationships that may exist between the full-sky and the partial-sky power spectrum of individual realizations of the CMB sky. Thus, to get a better estimate, we also replace the linear transformation with a functional relation while discarding the ensemble averages. Eq.11 can, then, be generalized as follows:

$$\mathbf{c}^{\text{estimate}} = f(\tilde{\mathbf{c}}). \quad (12)$$

The above equation can be equivalently described by the mapping problem,

$$\tilde{\mathbf{c}} \xrightarrow{f} \mathbf{c}. \quad (13)$$

Based on this expression, we explore a strategy using ANNs, discussed in §4, to approximate the full-sky CMB angular power spectrum.

3 Artificial Neural Networks

Artificial Neural Networks (ANNs) are computational information processing systems aimed at recognizing underlying relationships in a set of data. Historically, the learning mechanisms of neural networks have drawn inspiration from those of the human brain and the nervous system. However, as the study of neural networks progressed and various architectures that had little connection with the working of the brain were discovered, such comparisons are now debated. Even so, ANNs have found a wide range of applications ranging from financial predictions and function approximation to computer vision and speech recognition/synthesis. Bishop (1995) [26] gives a detailed description of neural networks.

In our work, we focus on supervised learning with ‘dense’ (fully-connected) feed-forward ANNs. An ANN consists of an input layer, an output layer and one or more hidden layers (see Fig.3). Each of the circular units is

called a neuron and the lines connecting the different neurons represent the associated weights. Consider the input features in a particular training example to be represented as a column vector \mathbf{x} whose elements are x_p ($p = 1, \dots, n_{\text{in}}$, where, n_{in} is the number of input features) and the true output values (or ground truths) to be represented as a column vector \mathbf{y} whose elements are \hat{y}_q ($q = 1, \dots, n_{\text{out}}$, where, n_{out} is the number of output values). An ANN can then be understood as a mapping from input to output,

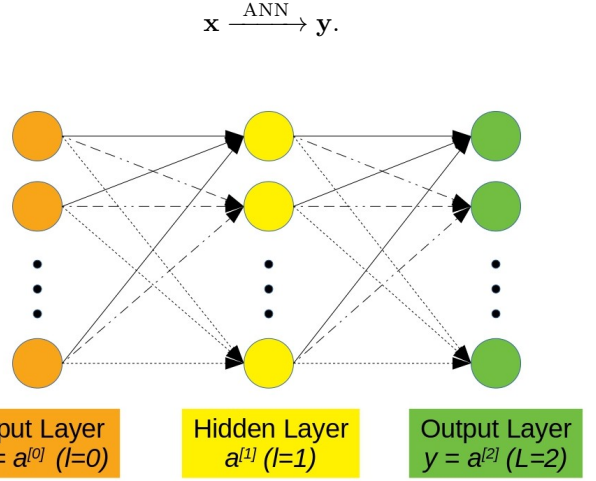


Figure 1: Figure showing a ‘dense’ ANN with an input layer, an output layer and a single hidden layer. The word ‘dense’ implies a fully-connected network in which all the neurons in any layer of the network are connected to all the neurons in the subsequent layer.

3.1 Forward Propagation

The ANN learns the mapping by training the weights and biases in the network. Each neuron in a layer is connected to all the neurons of the previous layer. We use the convention that superscript $[l]$ represents the l -th layer. Thus, any layer l has $n^{[l]}$ neurons, associated with $\mathbf{W}^{[l]}$ weights $[w_{ij}^{[l]}$ joining neuron i in layer l and neuron j in layer $(l-1)$] and $\mathbf{b}^{[l]}$ biases (or offsets) $[b_i^{[l]}$ of neuron i in layer l]. A neuron is comprised of a linear part and an activation part. Let the linear and activation parts of the neurons in the l -th hidden layer be represented as vectors $\mathbf{z}^{[l]}$ and $\mathbf{a}^{[l]}$, respectively. Then, the *forward propagation* step is given by,

$$z_i^{[l]} = \sum_{j=1}^{n^{[l-1]}} w_{ij}^{[l]} a_j^{[l-1]} + b_i^{[l]}, \quad (14)$$

$$a_i^{[l]} = g^{[l]}(z_i^{[l]}), \quad (15)$$

where $g^{[l]}(z)$ represents the activation function g of the l -th layer. The activation functions are chosen to be non-linear functions, e.g. logistic sigmoid, tanh, ReLU, etc., to introduce a non-linearity in the network. By convention, the input layer is referred to as the 0th layer, and $\mathbf{a}^{[0]} = \mathbf{x}$. The hidden layers, along with the activation functions, helps the ANN to create complex non-linear mappings.

For regression problems in which the output features are real-valued numbers, an identity activation is applied

to the output later. If the output layer is enumerated as L , the output layer activations can be computed as:

$$y_q = a_q^{[L]} = z_q^{[L]} = \sum_{j=1}^{n^{[L-1]}} w_{qj}^{[L]} a_j^{[L-1]} + b_q^{[L]}. \quad (16)$$

This constitutes the network's prediction vector \mathbf{y} which depends on the weights, biases, and activation functions of all the layers in the network, thus creating a complex mapping.

3.2 The Training Process

Consider training an ANN using m training examples of input and true output vector pairs $(\mathbf{x}^{(k)}, \hat{\mathbf{y}}^{(k)})$, where we use the convention that superscript (k) represents the k^{th} training example. The ANN *forward propagates* to get the neuron activations for all m training examples and eventually the predicted outputs $\mathbf{y}^{(k)}$ ($k = 1, \dots, m$). A training algorithm that minimizes a *cost function* (J) is used to train an ANN. For the real-valued output problem that we currently have at hand, we use the sum-of-squares error function averaged over all training examples as the *cost function*, i.e.,

$$J = \frac{1}{m} \sum_{k=1}^m \sum_{q=1}^{n_{\text{out}}} (y_q^{(k)} - \hat{y}_q^{(k)})^2. \quad (17)$$

A technique called *Error Back Propagation* [27] helps us estimate the gradients of the weights and biases w.r.t. the cost function based on all the training examples we consider. Taking a small step from w to $w + \delta w$ and from b to $b + \delta b$ changes the cost by an amount δJ , and we move in the direction in which J minimizes. This job of updating the parameters by a minimal amount in every iteration is handled by an *Optimization Algorithm*. Various types of optimization algorithms exist like *Gradient Descent*, *Stochastic Gradient Descent (SGD)*, *Momentum*, *RMSProp* [28], *Adaptive Moment Estimation (ADAM)* [29], etc. with their own sets of pros and cons. It is beyond the scope of this paper to provide a review of these, and we refer the reader to Sun et al. (2019) [30] for the same.

Updating the weights of a neural network by estimating the gradients based on all the training examples during each iteration of network-training may lead the neural network to get stuck in the local minima of the high-dimensional weight space. To tackle this problem, mini-batches of size b ($< m$) are used. The fluctuations in the weight space brought about by the mini-batch optimization algorithms like *Mini-batch Stochastic Gradient Descent (MSGD)*, *ADAM*, etc. by computing the gradients based on a subset of the entire training set during each iteration allow the neural network to jump to another possible minimum as shown by Ruder (2016) [31]. In literature, the terminology 'epoch' is used to address the number of iterations of the optimization algorithm, in which the network 'sees' all the training examples once.

$$1 \text{ epoch} = \lceil \frac{m}{b} \rceil \text{ iterations},$$

where b represents the number of training examples in a batch (i.e., batch-size) and $\lceil \circ \rceil$ represents the ceiling function.

The training process for the networks used can, thus, be summed up as follows:

1. Randomly initialize all the weights and initialize all the biases to zero.
2. Shuffle all the examples in the training set and split it into n_{bat} batches, each having b examples (except the last batch, which can have less than b examples).
3. (a) *Forward propagate* to get the neuron activations using the training examples in the considered batch.
- (b) Compute the *cost* on the current batch (J_r) as:

$$J_r = \sum_{k=1}^{\text{batch-size}} \sum_{q=1}^{n_{\text{out}}} (y_q^{(k)} - \hat{y}_q^{(k)})^2, \quad (18)$$

where the subscript r denotes the current batch.

- (c) *Back propagate* errors to get estimates of the gradients of the weight space, $\frac{\partial J_r}{\partial w}$ and $\frac{\partial J_r}{\partial b}$.
- (d) Update the weights and the biases using an optimization algorithm and the gradients.
- (e) Repeat steps 3a to 3d for all batches in the training set (i.e., $\lceil \frac{m}{b} \rceil$ iterations).
- (f) Compute the total *cost* (J_{tot}) as:

$$J_{\text{tot}} = \frac{1}{m} \sum_{r=1}^{n_{\text{bat}}} J_r \quad (19)$$

4. Repeat steps 2 and 3 for t number of epochs or till J_{tot} is minimized.

The hyper-parameters of the ANN model need to be tuned manually for training it successfully. While training, the performance on a separate validation set is tracked to ensure that the network does not over-fit to the training data. The ANN, with the trained weights and biases, is then used for making predictions on the test set. This way, it is ensured that testing is done on examples that the ANN has never seen before.

4 The Full-sky CMB Angular Power Spectrum Estimator

In view of the discussions in §2 and §3, Eq.13 is essentially the mapping problem that an ANN is designed to solve, i.e.,

$$\tilde{\mathbf{c}} \xrightarrow{\text{ANN}} \mathbf{c}, \quad (20)$$

when trained on data using $(\mathbf{x}^{(k)}, \hat{\mathbf{y}}^{(k)}) = (\tilde{\mathbf{c}}^{(k)}, \mathbf{c}^{(k)})$, where, $k = 1, \dots, m$ represent the m training examples. Partial-sky \hat{C}_l at all multipoles are required for estimating the full-sky \hat{C}_l at each multipole. Thus, we use 'dense' feed-forward ANNs to tackle this mapping problem.

A rich training data set, containing several realizations of the partial-sky and the full-sky spectra, is primary to training a good model for predicting the full-sky spectra from the partial-sky spectra. In the following sections, we will discuss how we obtain the simulated training data and build the network.

5 Simulations of the full-sky and partial-sky CMB angular power spectra

HEALPix [32] software¹ in python (`healpy`²) has been used to simulate and analyze random realizations of the CMB temperature anisotropy. `healpy.sphtfunc.synfast` can simulate full-sky CMB maps given the theoretical C_l^{th} . WMAP theoretical CMB temperature anisotropy power spectrum is used as the input theoretical C_l^{th} . The cosmological parameters used to generate this theoretical power spectrum model were the best-fitting parameters obtained using a standard Λ CDM model with a power-law spectral index [33]:

$$\{\Omega_b h^2, \Omega_m h^2, h, A, \tau, n_s\} = \{0.023, 0.13, 0.73, 0.8, 0.143, 0.97\}, \quad (21)$$

where, Ω_b is the baryonic energy density, Ω_m is the total matter density, h is the Hubble constant (in units of 100 km/s/Mpc), n_s is the scalar spectral index, τ is the optical depth to the decoupling surface, and A is the parameter used to characterise the amplitude of the initial perturbations.

We work with low resolution HEALPix maps at $N_{\text{side}} = 16$, which gives an angular resolution of ≈ 219.87 arcmin. At this resolution, only larger angular scale theoretical C_l^{th} up to $l_{\text{max}} = 32$ are provided as input to `synfast` for map generation. The simulated maps are also smoothed by a Gaussian beam with FWHM = 540 arcmin.

We present our analysis with two different masks. We use the ‘Kp2 mask’ as our first mask, in which $\approx 15\%$ of the pixels are masked. This mask is available as a WMAP product at $N_{\text{side}} = 512$, which is downgraded to $N_{\text{side}} = 16$. All the non-integer values that may have arisen due to downgrading are then rounded off to either 0 or 1. We use the temperature mask given alongside the Planck PR3 CMB IQU maps produced by the COMMANDER pipeline as our second mask, hereafter referred to as the ‘Planck T-mask’ ($\approx 12\%$ masked pixels). The mask is available at $N_{\text{side}} = 2048$, which is downgraded to $N_{\text{side}} = 16$ and applied with similar processing as described for the ‘Kp2 mask’. We apply these raw (1/0) masks (see Fig.2) to the random realizations of the CMB sky in order to get the masked CMB maps.

The angular power spectra (\hat{C}_l s) of the simulated full-sky maps are computed using `healpy.sphtfunc.anafast`, where we again set $l_{\text{max}} = 32$ as the maps were generated using the same l_{max} on C_l^{th} . However, in the case of partial-sky maps, we compute the angular power spectra (\hat{C}_l s) with $l_{\text{max}} = 47$ so as to extract as much information as possible from the masked maps, which would assist our ANNs in making better predictions. CMB \hat{C}_l are usually plotted as $l(l+1)\hat{C}_l/2\pi$, following which a lot of the structure at smaller scales is brought out. The power spectra are also divided by an additional factor of $B_l^2 P_l^2$, where B_l represents the beam window function of the Gaussian beam corresponding to FWHM = 540 arcmin and P_l represents the pixel window function for $N_{\text{side}} = 16$, so as

to account for the effects of smoothing and pixel area, respectively. Fig.3 depicts the procedure for obtaining the required data for a realization of the CMB sky.

Following the procedure, 1.2×10^5 random realizations of the CMB sky are simulated, getting the angular power spectra of which give us 1.2×10^5 examples of full-sky CMB \hat{C}_l . Then, each of these full-sky maps are masked with the ‘Kp2 mask’ and the angular power spectra are computed to get the corresponding 1.2×10^5 examples of partial-sky CMB \hat{C}_l . Further, each of the full-sky maps is then masked with the ‘Planck T-mask’ to get the corresponding 1.2×10^5 examples of partial-sky CMB \hat{C}_l . This is the simulated data that we use to train the neural networks.

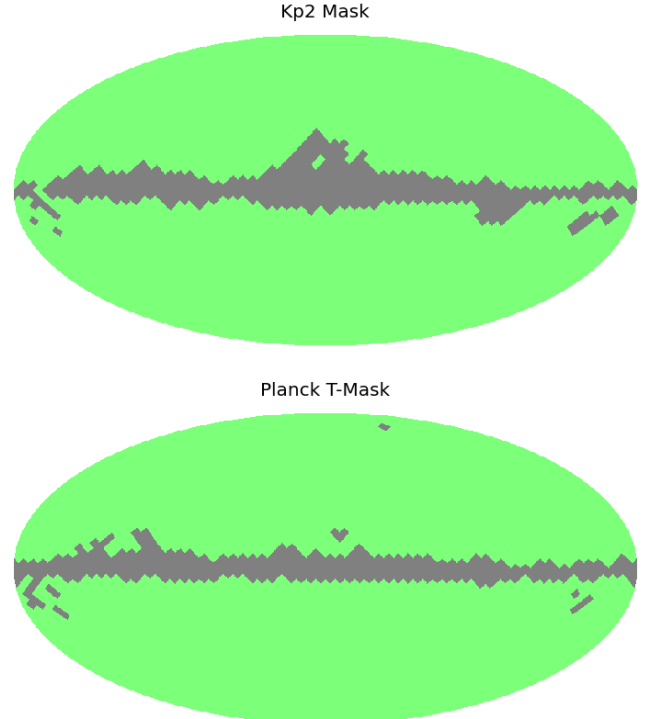


Figure 2: The Kp2 mask and the Planck T-mask at $N_{\text{side}} = 16$ that we use for our analyses. The masked region of the sky is shown in gray colour and the unmasked region is shown in green colour.

6 Training the networks and making predictions

Due to the statistical nature of the problem, it is known that the neural network needs to ‘see’ at least 10^5 training examples so as to map possible feature variations. Out of the 1.2×10^5 pairs of examples of the full-sky \hat{C}_l and the partial-sky \hat{C}_l obtained using the ‘Kp2 mask’, 10^5 pairs of $(\tilde{\mathbf{c}}, \mathbf{c})$ are designated as the training set, while 10^4 pairs each are kept aside as validation and test sets. A similar train, validation, and test set splitting is done for $(\tilde{\mathbf{c}}, \mathbf{c})$ pairs obtained using the ‘Planck T-mask’.

We train two different neural networks - 1. For estimating full-sky \hat{C}_l using partial-sky \hat{C}_l obtained with the ‘Kp2 mask’, and 2. For estimating full-sky \hat{C}_l using partial-sky

¹<https://healpix.sourceforge.io/>

²<https://github.com/healpy/healpy>

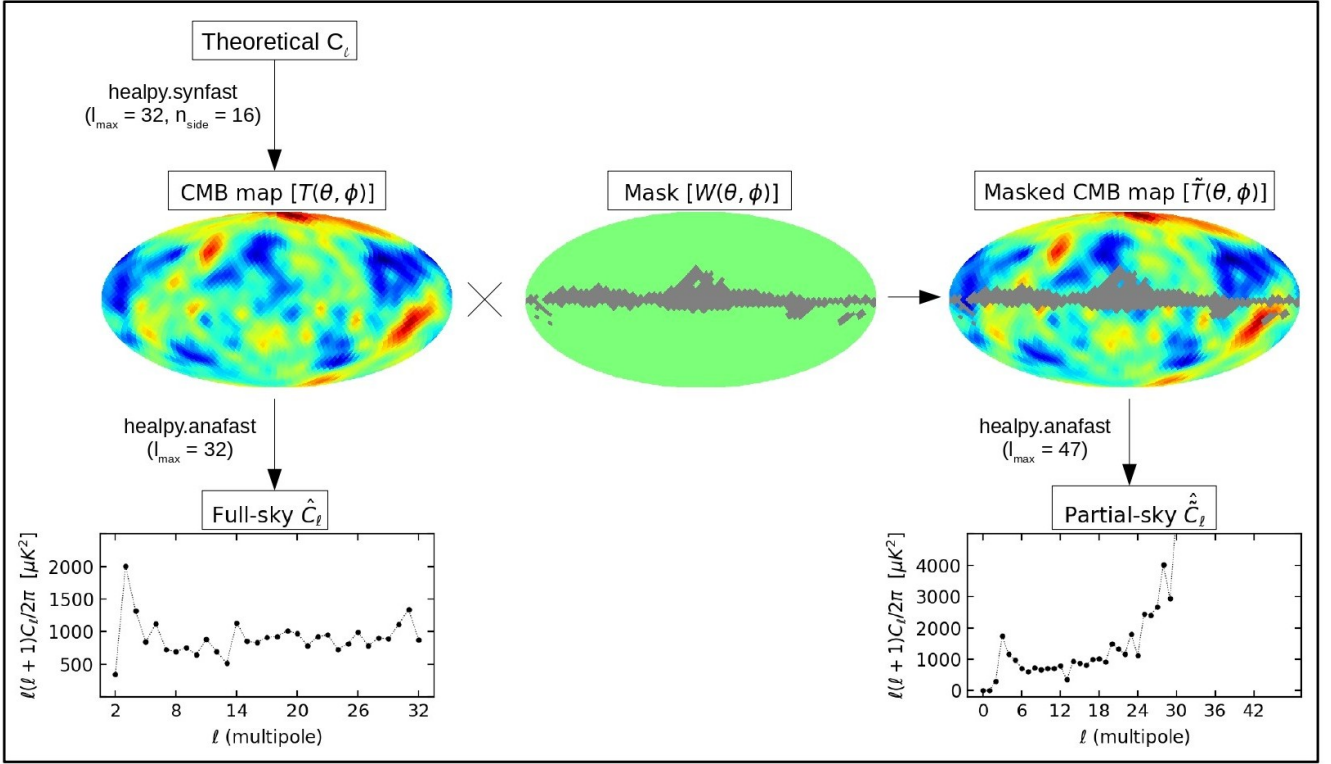


Figure 3: Figure showing the procedure for generating the simulated data at $N_{\text{side}} = 16$. A realization of the CMB sky is obtained given the theoretical power spectrum, C_l^{th} . Its angular power spectrum gives the \hat{C}_l . The desired mask is then applied on the CMB map. The angular power spectrum of the masked CMB map gives the $\hat{\tilde{C}}_l$. The $\hat{\tilde{C}}_l$ are very large at higher multipoles due to the loss of information caused by masking.

$\hat{\tilde{C}}_l$ obtained with the ‘Planck T-mask’. Here forth, we refer to the analyses using the ‘Kp2 mask’ and ‘Planck T-mask’ as cases I and II, respectively. For both ANNs, the input features are $\mathbf{x} = \tilde{\mathbf{c}}$ (generated using the corresponding mask), and the true output values are $\hat{\mathbf{y}} = \mathbf{c}$, as discussed in §4. Considering the discussion in §5 and noting that the \hat{C}_l at $l = 0, 1$ provide no useful information and can consequently be discarded, our input and output feature vectors have 48 and 31 dimensions, respectively, i.e., our input partial-sky spectra have $l_{\text{max}} = 47$, and we predict the full-sky spectra in the multipole range: $2 \leq l \leq 32$.

We have used TENSORFLOW³ [34] machine-learning framework to set up, train, and analyze the neural networks. Training the networks is an iterative procedure. Mean normalization pre-processing is applied on the input features of the training set for both cases. This transforms all our input training features to have a similar range and allows the optimization algorithm to efficiently explore the weight-space. The mean and scale used to transform the training set are also used to process the validation and test sets to ensure that the prediction features go through the same pre-processing as the training ones. This helps to accurately estimate the network reliability.

An ANN with two hidden layers having 64 neurons each with ReLU activation is found to work best for both cases. The training takes about 2 CPU hours on a personal computer with Intel® Core™ i5-6200U (@ 2.30GHz×4, 8 GB RAM). The schematic of the ANN architecture used in this work is shown in Fig.4. We use ADAM as our op-

timization algorithm and use mini-batches while training the ANNs. The performance of the ANNs on the corresponding validation sets are also tracked.

After training the networks and getting the predictions on the test sets, we bin the predicted full-sky spectra $l = 21$ onward with a bin width of two to get an unbiased estimate at larger multipoles. Thus, six bins are obtained from $21 \leq l \leq 32$. The binned \hat{C}_l is assigned to the central multipole of the corresponding bin.

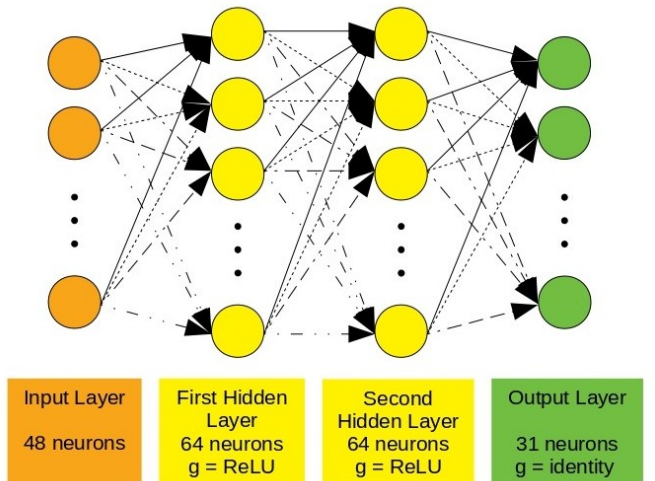


Figure 4: Representation of the ANN architecture that we use for our analyses. The ANN has an input layer with 48 neurons, an output layer with 31 neurons, and two hidden layers with 64 neurons each and ReLU activation function.

³<https://www.tensorflow.org/>

7 Results

In this section, we discuss the results from simulations depicting the use of the two different masks. We mask each of the simulated CMB maps once with the Kp2 mask and once with the Planck T-mask, get the required power spectra, and create the corresponding training, validation, and test sets using the procedure described in §5. The trained ANNs are utilized to predict the full-sky CMB angular power spectra on the corresponding test sets (see §6).

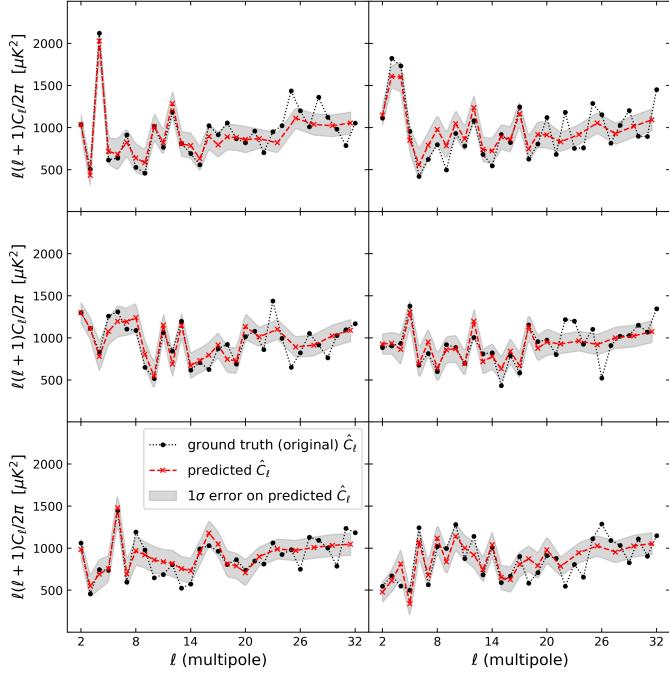


Figure 5: Some examples of full-sky \hat{C}_l predictions made by ANN in case I, i.e., for the analysis with the Kp2 mask. The predictions are in good agreement with the ground truths at lower multipoles. At higher multipoles, the predictions smoothen out compared with the ground truths.

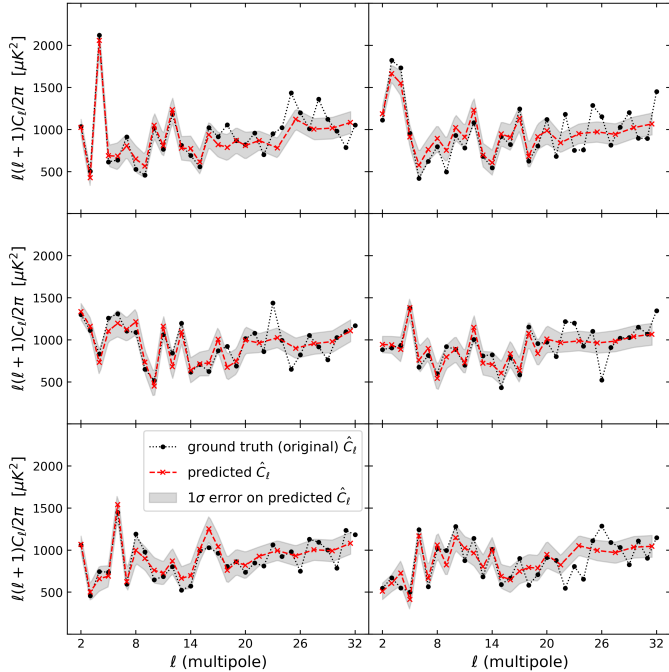


Figure 6: Same as Figure 5 but for case II, i.e., the analysis with the Planck T-mask.

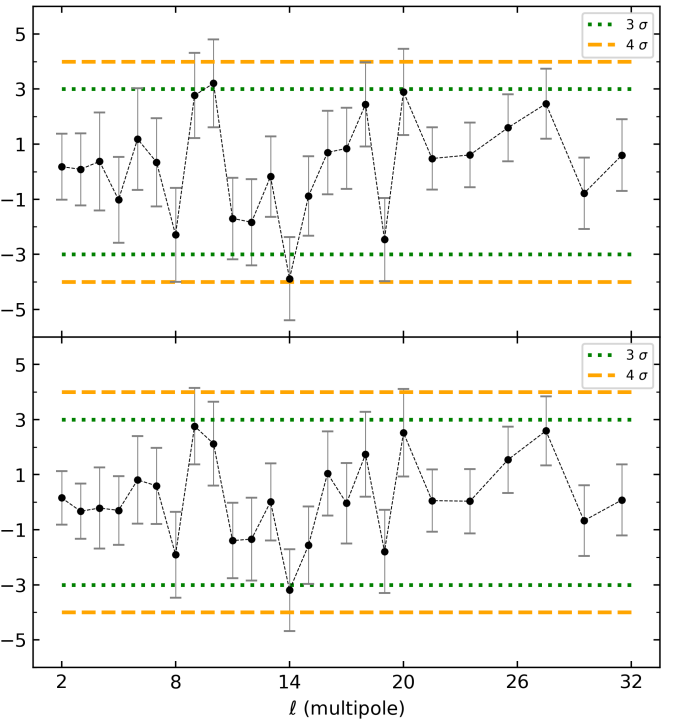


Figure 7: Figure showing the mean and the SEM of the $10^4 \hat{C}_l$ differences ($\mathbf{c}^{\text{original}} - \mathbf{c}^{\text{predicted}}$) for case I, i.e., when the Kp2 mask is used (top), and for case II, i.e., when the Planck T-mask is used (bottom). The mean is less than 3σ at all of the multipoles except at $l = 10, 14$ when using the Kp2 mask and at $l = 14$ when using the Planck T-mask, where it is between 3σ and 4σ .

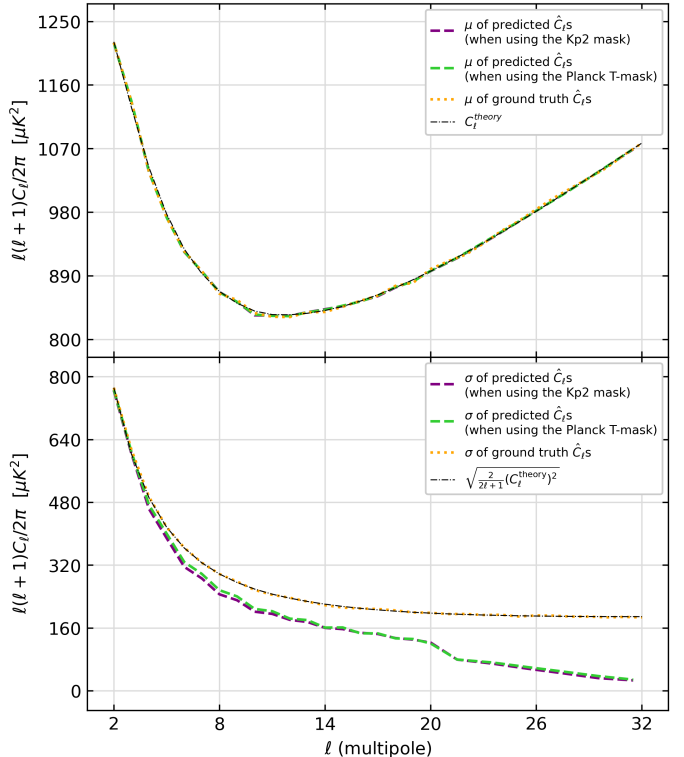


Figure 8: Figure showing the statistics - mean (top) and standard deviation (bottom) - of the predicted full-sky \hat{C}_l s and those of the ground truths for the analyses with both masks. The theoretically expected statistics are also shown. The mean of the predictions are in good agreement with C_l^{th} . The standard deviation of the predictions is smaller than the square root of the cosmic variance.

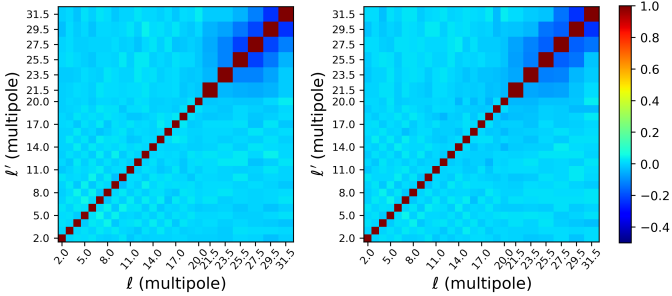


Figure 9: Correlation matrices of the predicted full-sky \hat{C}_l s for case I, i.e., for the analysis with the Kp2 mask (left), and for case II, i.e., for the analysis with the Planck T-mask (right). The correlations are negligible at lower multipoles. Some correlations are present at higher multipoles. The correlations obtained when using the Planck T-mask are lower than those obtained with the Kp2 mask.

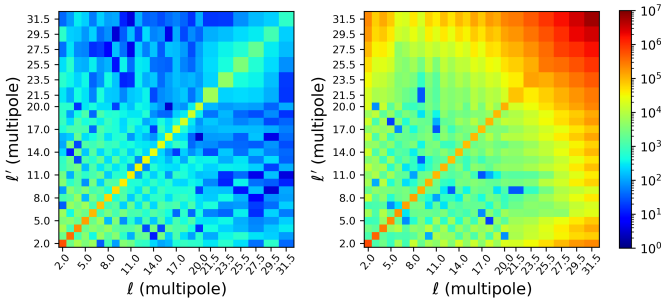


Figure 10: Left panel: Covariance matrix of the predicted \hat{C}_l s using ANN for case I, i.e., when the Kp2 mask is used. The matrix shows that the predictions have some covariance at lower multipoles and in a region around the diagonal at higher multipoles, while the covariances are much lower in the remaining areas. Right panel: Covariance matrix of the estimated \hat{C}_l s using the pseudo- C_l method with the Kp2 mask. The matrix has a smooth structure with the covariances being larger at higher multipoles. Overall, the covariances observed in pseudo- C_l estimates are larger than those obtained using the ANN predictions.

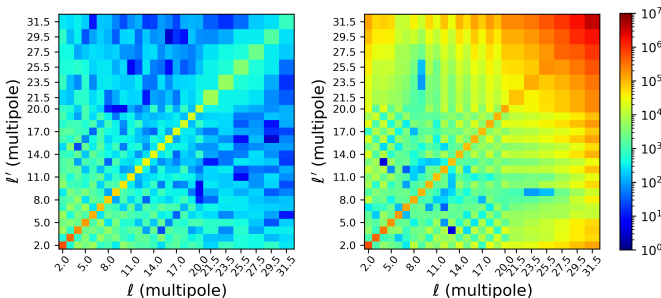


Figure 11: Same as Figure 10 but for case II, i.e., when the Planck T-mask is used.

Fig.5 and Fig.6 show some predictions of the full-sky angular power spectrum made by the ANNs on the test sets along with the ground truth (original) power spectrum for cases I and II, respectively. At lower multipoles, the \hat{C}_l predictions of the neural networks almost trace the original \hat{C}_l . The mask leads to a greater loss of information at higher multipoles (see Fig.3), and consequently, we observe that the ANNs are unable to reconstruct the features or fluctuations in the power spectra efficiently. However, being intelligent systems, the ANNs compensate for the information loss and predict the full-sky \hat{C}_l increasingly

closer to C_l^{th} at larger multipoles, even though the ANNs are not provided with any information about the same.

The power spectra differences ($\mathbf{c}^{\text{original}} - \mathbf{c}^{\text{predicted}}$) for the 10^4 examples in the corresponding test sets are obtained. Fig.7 plots the mean of these differences along with the standard error of the mean (SEM) for cases I and II, respectively. In both cases, the mean of the \hat{C}_l differences are below 3σ at most of the multipoles. At $l = 10, 14$ for case I and at $l = 14$ for case II, the mean of the \hat{C}_l differences are between 3σ and 4σ . This indicates that the predictions of the full-sky spectra are unbiased.

We compute the overall statistics of the predictions and compare them with those of ground truths and the theoretical C_l^{th} in Fig.8. The mean of the 10^4 predicted full-sky \hat{C}_l s traces the C_l^{th} and the mean of original ground truth \hat{C}_l s in both cases. However, the standard deviation of the predictions is less than the square root of the cosmic variance and the standard deviation of the ground truths. The most likely reason for this is the same as discussed earlier, the predictions made by the ANN are progressively closer to the mean, C_l^{th} , as the multipoles increase so as to make up for the loss of information due to masking and not go arbitrarily wrong on the predictions. The standard deviations of the predictions also have a small dip caused by the binning of the predicted \hat{C}_l $l = 21$ onwards.

We further present the correlation matrices of the full-sky \hat{C}_l predicted by the ANNs for cases I and II in Fig.9. The correlations are almost absent at lower multipoles up to $l \lesssim 22$. The higher multipoles have a maximum correlation of about 24% near the last three bins, with the other correlations being less than $\approx 12\%$. Overall, the correlations are lower in case II compared with case I. This is likely because there are $\approx 3\%$ lesser masked pixels in the Planck T-mask than the Kp2 mask, which leads to somewhat more information in the corresponding \hat{C}_l . The corresponding ANN is able to use this information to make predictions with comparatively lesser correlations.

Finally, the covariance matrices of the predictions made by the ANN and the estimations given by the method of pseudo- C_l on the test sets for cases I and II are shown side by side for comparison in Fig.10 and Fig.11, respectively. We discern that the covariance matrices for the two methods are structured differently from one another, with the covariances being significantly smaller with our method using ANNs for both cases I and II.

8 Discussions and Conclusions

In this paper, we have demonstrated for the first time that supervised machine learning with Artificial Neural Networks can be employed to estimate the full-sky CMB angular power spectrum (\hat{C}_l) effectively from the partial-sky spectrum ($\hat{\hat{C}}_l$).

We have considered two different masks in our analysis - the Kp2 mask and the Planck T-mask. We have exhibited that an ANN with just two hidden layers can be utilized for the purpose. The optimum number of layers and neurons in a layer were found by training various neural network architectures until we got the best results for both cases. We have not used detector noise in our simu-

lations, which is a reasonable assumption for temperature and power spectrum analysis over large angular scales at $N_{\text{side}} = 16$.

Both masks conceal comparable regions of the sky. The predictions made by the ANNs on the corresponding test sets show that the estimations are equally good (see Fig.5 and Fig.6). The mean and the SEM of the $10^4 \hat{C}_l$ differences ($\mathbf{c}^{\text{original}} - \mathbf{c}^{\text{predicted}}$) on our test sets for both cases also show that the full-sky \hat{C}_l predictions are unbiased (see Fig.7). By comparing the overall statistics of the predictions with those of the ground truths and C_l^{th} , we have shown that our ANN does not output negative or arbitrarily high full-sky power spectra at higher multipoles where the information loss due to the cut-sky is significant. This helps us accurately recover the mean C_l^{th} , while obtaining a decent unbiased estimate of the \hat{C}_l s even at larger multipoles. However, the ANN predictions are not able to fully recover the cosmic variance on the test sets. Preserving the cosmic variance on the \hat{C}_l predictions will be the subject of a subsequent study of this ANN method.

The correlation matrices of the predicted full-sky spectra in both analyses (see Fig.9) suggest that the \hat{C}_l predictions are mostly uncorrelated with some residual correlation at higher multipoles where the partial-sky spectra are extremely correlated owing to the loss of information on the cut-sky. We have also compared the covariance matrices of the full-sky spectra predictions made by the ANNs and the full-sky spectra estimates obtained using the pseudo- C_l method (see Fig.10 and Fig.11), which indicate that the ANNs obtain significantly smaller covariances on the predictions at all multipoles compared to the latter method in both cases I and II. However, we restate that the ANNs achieve this at the cost of a lesser variance on the \hat{C}_l predictions compared with the cosmic variance.

Nonetheless, our initial analysis has produced encouraging results and exemplifies the capacity of ANNs as a new alternative method for estimation of the full-sky CMB angular power spectra. Further research is needed in this area in order to improve the method and make the predictions better. A project focused on a higher resolution analysis that includes instrumental noise would be particularly interesting. A useful advantage of our method is that it does not require a machine with very high computational power. Even for a higher resolution analysis, ANNs will be reliably fast in convergence, as the ANNs can compute complex functional mappings between high dimensional input and output features by using just a few layers and neurons in the network with much-advanced optimization algorithms.

We have presented an unbiased estimator of the full-sky \hat{C}_l from the partial-sky \hat{C}_l and accurately recovered the C_l^{th} using neural networks in this article. Going forward, we would like to probe the reliability of the full-sky spectra predictions made by the neural networks in measurements of the cosmological parameters and the application of this developed ANN framework for cosmological analyses.

Acknowledgements

The authors would like to thank Vipin Sudevan for their help. P.C. would like to thank Nirnay Roy and Prashant Shukla for their help and insightful discussions at various stages of this work. P.C. would also like to acknowledge the support of DST for providing the INSPIRE scholarship. The authors would like to acknowledge the use of open-source packages HEALPIX⁴ and TENSORFLOW⁵, and thank the respective groups for the same.

References

- [1] Charles L Bennett, Anthony J Banday, et al. Four-year cobe* dmr cosmic microwave background observations: maps and basic results. *The Astrophysical Journal Letters*, 464(1):L1, 1996.
- [2] CL Bennett, RS Hill, et al. First-year wilkinson microwave anisotropy probe (wmap)* observations: Foreground emission. *The Astrophysical Journal Supplement Series*, 148(1):97, 2003.
- [3] Peter AR Ade, N Aghanim, et al. Planck 2013 results. xvi. cosmological parameters. *Astronomy & Astrophysics*, 571:A16, 2014.
- [4] Jonathan L Sievers, Renee A Hlozek, et al. The atacama cosmology telescope: Cosmological parameters from three seasons of data. *Journal of Cosmology and Astroparticle Physics*, 2013(10):060, 2013.
- [5] Z Hou, CL Reichardt, et al. Constraints on cosmology from the cosmic microwave background power spectrum of the 2500 deg² spt-sz survey. *The Astrophysical Journal*, 782(2):74, 2014.
- [6] GJ Stacey, M Aravena, et al. Ccat-prime: science with an ultra-widefield submillimeter observatory on cerro chajnantor. In *Ground-based and Airborne Telescopes VII*, volume 10700, page 107001M. International Society for Optics and Photonics, 2018.
- [7] P. de Bernardis, P.A.R. Ade, et al. Exploring cosmic origins with CORE: The instrument. *Journal of Cosmology and Astroparticle Physics*, 2018(04):015–015, apr 2018.
- [8] Arno A Penzias and Robert Woodrow Wilson. A measurement of excess antenna temperature at 4080 mc/s. *The Astrophysical Journal*, 142:419–421, 1965.
- [9] DJ Fixsen, ES Cheng, et al. The cosmic microwave background spectrum from the full cobe* firas data set. *The Astrophysical Journal*, 473(2):576, 1996.
- [10] H. K. Eriksen, I. J. O'Dwyer, et al. Power Spectrum Estimation from High-Resolution Maps by Gibbs Sampling. *ApJS*, 155(2):227–241, December 2004.
- [11] H. K. Eriksen, J. B. Jewell, et al. Joint Bayesian Component Separation and CMB Power Spectrum Estimation. *ApJ*, 676(1):10–32, March 2008.
- [12] Rajib Saha, Pankaj Jain, and Tarun Souradeep. A blind estimation of the angular power spectrum of CMB anisotropy from WMAP. *The Astrophysical Journal*, 645(2):L89–L92, jul 2006.
- [13] Rajib Saha, Simon Prunet, et al. Cmb anisotropy power spectrum using linear combinations of wmap maps. *Phys. Rev. D*, 78:023003, Jul 2008.
- [14] Vipin Sudevan and Rajib Saha. A global ILC approach in pixel space over large angular scales of the sky using CMB covariance matrix. *The Astrophysical Journal*, 867(1):74, nov 2018.
- [15] J. R. Bond, A. H. Jaffe, and L. Knox. Estimating the power spectrum of the cosmic microwave background. *Phys. Rev. D*, 57:2117–2137, Feb 1998.
- [16] Benjamin D. Wandelt and Frode K. Hansen. Fast, exact cmb power spectrum estimation for a certain class of observational strategies. *Phys. Rev. D*, 67:023001, Jan 2003.
- [17] Justin Alsing, Alan Heavens, et al. Hierarchical cosmic shear power spectrum inference. *Monthly Notices of the Royal Astronomical Society*, 455(4):4452–4466, 12 2015.
- [18] Frode K Hansen, Krzysztof M Górska, and Eric Hivon. Gabor transforms on the sphere with applications to cmb power spectrum estimation. *Monthly Notices of the Royal Astronomical Society*, 336(4):1304–1328, 2002.

⁴<https://healpix.sourceforge.io/>

⁵<https://www.tensorflow.org/>

[19] P. J. E. Peebles. Statistical Analysis of Catalogs of Extragalactic Objects. I. Theory. *ApJ*, 185:413–440, October 1973.

[20] Benjamin D. Wandelt, Eric Hivon, and Krzysztof M. Gorski. Cosmic microwave background anisotropy power spectrum statistics for high precision cosmology. *Phys. Rev. D*, 64:083003, Sep 2001.

[21] Eric Hivon, Krzysztof M. Gorski, et al. Master of the cosmic microwave background anisotropy power spectrum: A fast method for statistical analysis of large and complex cosmic microwave background data sets. *The Astrophysical Journal*, 567(1):2–17, Mar 2002.

[22] Reinecke, M. and Seljebotn, D. S. Libsharp - spherical harmonic transforms revisited. *A&A*, 554:A112, 2013.

[23] Franz Elsner, Boris Leistedt, and Hiranya V. Peiris. Unbiased methods for removing systematics from galaxy clustering measurements. *Monthly Notices of the Royal Astronomical Society*, 456(2):2095–2104, 12 2015.

[24] Kurt Hornik. Approximation capabilities of multilayer feedforward networks. *Neural Networks*, 4(2):251 – 257, 1991.

[25] Allan Pinkus. Approximation theory of the mlp model in neural networks. *Acta Numerica*, 8:143–195, 1999.

[26] Christopher M Bishop et al. *Neural networks for pattern recognition*. Oxford university press, 1995.

[27] Robert Hecht-Nielsen. Theory of the backpropagation neural network. In *Neural networks for perception*, pages 65–93. Elsevier, 1992.

[28] G Hinton, N Srivastava, and K Swersky. Neural networks for machine learning—lecture 6e—rmsprop: Divide the gradient by a running average of its recent magnitude. *URL: https://www.cs.toronto.edu/tijmen/csc321/slides/lectureslideslec6.pdf*, 2012.

[29] Diederik P Kingma and Jimmy Ba. Adam: A method for stochastic optimization. *arXiv preprint arXiv:1412.6980*, 2014.

[30] S. Sun, Z. Cao, et al. A survey of optimization methods from a machine learning perspective. *IEEE Transactions on Cybernetics*, 50(8):3668–3681, 2020.

[31] Sebastian Ruder. An overview of gradient descent optimization algorithms. *arXiv preprint arXiv:1609.04747*, 2016.

[32] Krzysztof M Gorski, Eric Hivon, et al. Healpix: A framework for high-resolution discretization and fast analysis of data distributed on the sphere. *The Astrophysical Journal*, 622(2):759, 2005.

[33] David N Spergel, Licia Verde, et al. First-year wilkinson microwave anisotropy probe (wmap)* observations: determination of cosmological parameters. *The Astrophysical Journal Supplement Series*, 148(1):175, 2003.

[34] Martín Abadi, Ashish Agarwal, et al. TensorFlow: Large-scale machine learning on heterogeneous systems, 2015. Software available from tensorflow.org.